COMMUNICATION

ADVANCED
MATERIALS

www.advmat.d

Check for
updates

3D-Printable Fluoropolymer Gas Diffusion Layers for CO$_2$ Electroreduction

Joshua Wicks, Melinda L. Jue, Victor A. Beck, James S. Oakdale, Nikola A. Dudukovic, Auston L. Clemens, Siwei Liang, Megan E. Ellis, Geonhui Lee, Sarah E. Baker, Eric B. Duoss,* and Edward H. Sargent*

The electrosynthesis of value-added multicarbon products from CO$_2$ is a promising strategy to shift chemical production away from fossil fuels. Particularly important is the rational design of gas diffusion electrode (GDE) assemblies to react selectively, at scale, and at high rates. However, the understanding of the gas diffusion layer (GDL) in these assemblies is limited for the CO$_2$ reduction reaction (CO$_2$RR): particularly important, but incompletely understood, is how the GDL modulates product distributions of catalysts operating in high current density regimes > 300 mA cm^{-2}. Here, 3D-printable fluoropolymer GDLs with tunable microporosity and structure are reported and probe the effects of permeance, microstructural porosity, macrostructure, and surface morphology. Under a given choice of applied electrochemical potential and electrolyte, a 100× increase in the C$_2$H$_4$:CO ratio due to GDL surface morphology design over a homogeneously porous equivalent and a 1.8× increase in the C$_2$H$_4$ partial current density due to a pyramidal macrostructure are observed. These findings offer routes to improve CO$_2$RR GDEs as a platform for 3D catalyst design.

Utilizing carbon dioxide (CO$_2$) emissions to create value-added products is an attractive approach to reduce net greenhouse gas emissions.[1–3] In particular, processes such as the electrochemical reduction of CO$_2$ to ethylene (C$_2$H$_4$) and ethanol (C$_2$H$_5$OH) offer a pathway to producing commodity chemicals without fossil fuels when they are powered using low-carbon electricity. While traditional H-cell reactors have been widely used in the field of electrochemistry to study the CO$_2$ reduction reaction (CO$_2$RR), they are mass-transport limited as a result of the low solubility of CO$_2$ in the electrolyte.[4,5] This reduces the productivity, or current density—the rate at which the reaction can proceed. Furthermore, as a batch process, it precludes the scale-up of the reaction.

Recent strategies to overcome these mass-transport limitations include flow cell and membrane electrode assembly (MEA) configurations,[6–8] in which CO$_2$ diffuses through a porous substrate—the gas diffusion layer (GDL)—to meet the solid-phase catalyst and liquid/solid electrolyte at this multiphase interface. The GDL must also provide adequate hydrophobicity such that flooding by the electrolyte is prevented, and water is managed.[9] Commercially available GDLs include polytetrafluoroethylene (PTFE)-coated carbon paper substrates with microporous layers, and fibrous expanded PTFE (ePTFE). However, the control over pore size, macroscale structure, and resultant gas flow through these conventional GDLs is limited.

While studied extensively in fuel cell research,[10–12] the GDL is less explored in flow reactors for CO$_2$RR. Notably, recent developments have identified the influence of overlayers at the catalyst:electrolyte interface to enhance ethylene or ethanol production.[13,14] The CO$_2$ concentration in the local electrochemical environment of catalytic sites has also been shown to affect the product distribution of copper catalysts.[15] Parameters such as the catalyst layer thickness and porosity, CO$_2$ feed concentration, and feed flow rate are avenues to tune the local CO$_2$ concentration, and thus control the product distribution.[16] However, beyond the electrosynthesis of CO from CO$_2$,[17] the implications of GDL design to CO$_2$RR targeting multicarbon (C$_{2+}$) products are not yet fully understood. The GDL is not expected to affect intrinsic catalytic properties, but rather modulate the transport of gaseous reactants (CO$_2$) and products (CO, CH$_4$, C$_2$H$_4$) to and away from the catalyst layer, consequently altering selectivity. CO is a particularly interesting species as it can undergo the CO reduction reaction (CORR), is a reaction intermediate for C—C coupling, and uses the same Cu catalyst as CO$_2$RR to make C$_{2+}$ products.[18,19]

With this in mind, we developed a porous fluoropolymer system that meets the porosity and hydrophobicity requirements of GDLs while imparting additional 3D printing capabilities. We use this tunable material to investigate how structural parameters such as porosity, microstructure, and macrostructure impact species transport and further modulate the product distribution during CO$_2$RR. We then deploy these insights to

J. Wicks, G. Lee, Prof. E. H. Sargent
Department of Electrical and Computer Engineering
University of Toronto
35 St. George Street, Toronto, Ontario M5S 1A4, Canada
E-mail: ted.sargent@utoronto.ca
Dr. M. L. Jue, Dr. V. A. Beck, Dr. J. S. Oakdale, Dr. N. A. Dudukovic,
A. L. Clemens, Dr. S. Liang, M. E. Ellis, Dr. S. E. Baker, Dr. E. B. Duoss
Lawrence Livermore National Laboratory
7000 East Avenue, Livermore, CA 94550, USA
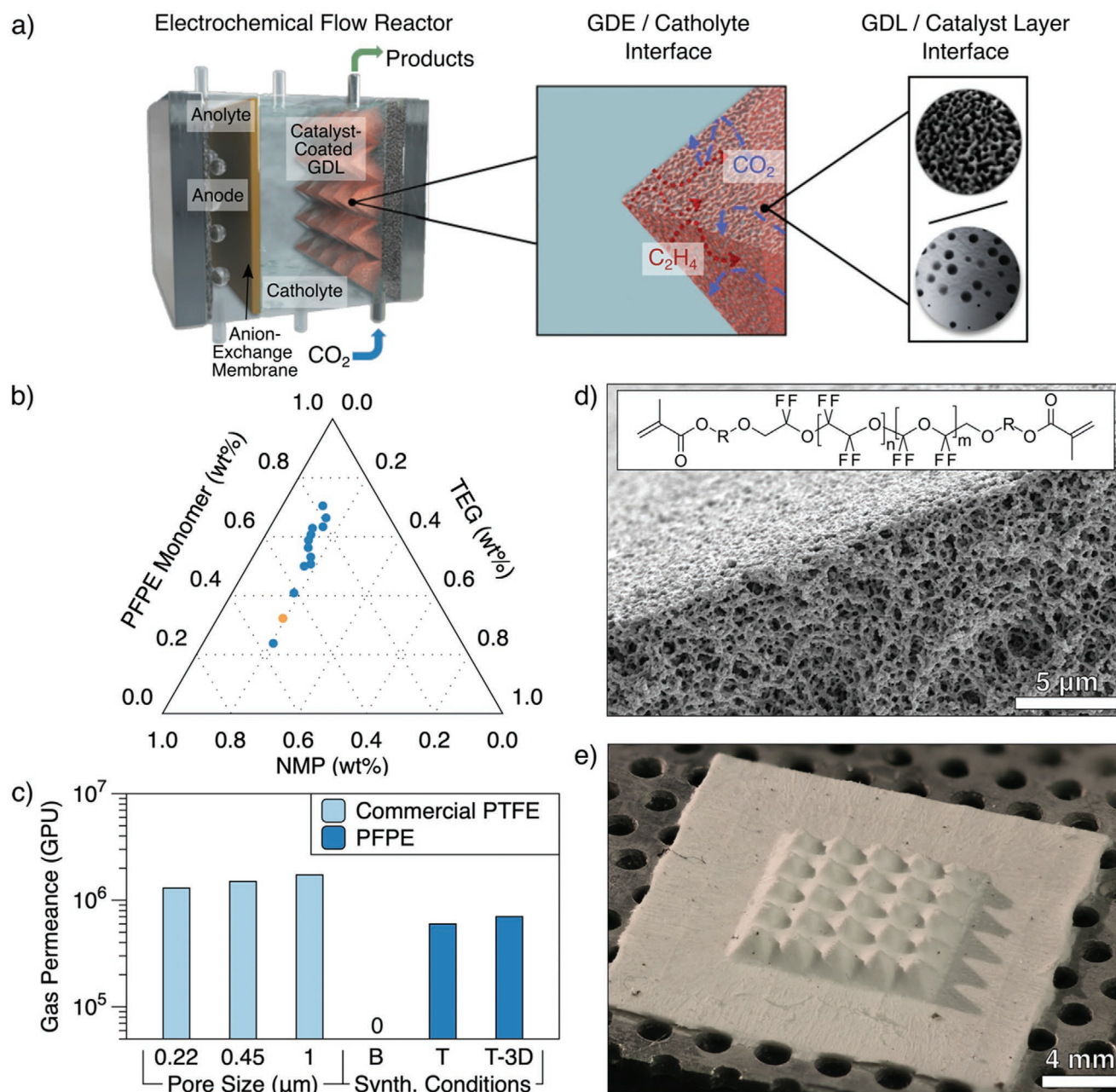E-mail: duoss1@llnl.gov

The ORCID identification number(s) for the author(s) of this article can be found under https://doi.org/10.1002/adma.202003855.

Figure 1. PFPE polymer development. a) Full electrochemical flow cell schematic highlighting a 3D gas diffusion layer (GDL) with a conformal copper nanoparticle catalyst (left). The macrostructure interface between the flowing catholyte and the gas diffusion electrode (GDE); the gaseous CO_2 reactant and C_2H_4 product of interest are highlighted (middle). The diffusive pathways of these gaseous components through the GDE are shown by the dotted arrows. Surface morphology at the GDL/catalyst interface (right) is shown: Homogeneous (H)-PFPE (top) and large pore (LP)-PFPE (bottom). b) Ternary phase diagram for mixtures of PFPE monomer, N-methyl-2-pyrrolidone (NMP), and triethylene glycol (TEG). Composition used to fabricate the membrane in part d) is in yellow (33 wt% PFPE). c) Hydraulic CO_2 permeance through commercial ePTFE materials of varying nominal pore size compared to PFPE porous materials fabricated from binary (B), ternary (T), and 3D-printed ternary (T-3D) synthesis conditions. d) PFPE chemical structure and SEM image of the top edge of the porous H-PFPE. e) 3D-printed ternary GDL used in this work (H-Δ-PFPE-1.6).

create the first 3D-printed fluoropolymer gas diffusion electrodes (GDE, **Figure 1**a) by coating a conformal Cu catalyst layer (CL) on the structured GDL.

Recently, Rapp et al. described a superhydrophobic porous coating derived from perfluoropolyether (PFPE) networks obtained through UV curing diacrylate monomers dissolved in fluorocarbon solvents.[20,21] These PFPE monomers are commercially available with a variety of reactive end groups and have been described and utilized for their hydrophobicity in many applications including paints, coatings, and soft lithography.[22,23] Inspired by this work, we developed monolithic, free-standing, porous PFPE GDLs that utilize nonvolatile

benign solvents amenable to 3D printing. The chemical structure of the PFPE monomer used here is shown alongside an SEM image of the resulting homogenously porous PFPE polymer in Figure 1d.

Monomer solution composition and curing conditions are intimately related to the physical and transport properties of these highly tunable PFPE polymers. Radical-mediated thermal or UV-curing of neat PFPE diacrylate monomers results in an impermeable hydrophobic material. However, porosity can easily be imparted into the otherwise dense polymer matrix by incorporating a pore-forming agent, or porogen.[8] While binary PFPE monomer/porogen systems have been investigated, the ones explored here produced impermeable GDLs; detailed monomer solution development is discussed in Figure S1 (Supporting Information). Ternary solutions consisting of a monomer and two porogens with compositions at the cloud point— the intermediate region between the one-phase and two-phase regions on the solution phase diagram (Figure 1b)[24]—produced UV-cured membranes with permeances on par with commercially available materials like ePTFE (Figure 1c). This homogenous PFPE (H-PFPE), shown in Figures 1d and 2a,b, was formed using low intensity ($\approx$5 mW cm^{-2}, 365 nm) UV light to create a uniform, highly porous, and well-interconnected

skeletal polymer network as has been described for other photopolymerized monomer/porogen systems.[25] Utilizing nonvolatile porogens in this way allows the creation of a variety of structures through conventional and advanced manufacturing methods (Figure 1e and Figure S4, Supporting Information). All material configurations were shown to be hydrophobic through water contact angle (WCA) analysis (Figure S9, Supporting Information).

The relationship between GDL porosity, permeance, and CO$_2$RR performance is relevant to CO$_2$ delivery to the catalyst layer. Controlling the PFPE monomer concentration at the cloud point, while maintaining a consistent internal microstructure, gives experimental access to a simple physical tuning parameter to modulate the CO$_2$ permeance over four orders of magnitude (Figure 2c). To connect PFPE synthesis parameters to the CO$_2$RR product distribution, we implemented a copper nanoparticle catalyst layer that has been shown to enable high current densities. This formulation extends CO$_2$ availability to a maximal number of catalytically active Cu sites through an intimate integration of perfluorosulfonic acid (PFSA) ionomers within the catalyst layer.[26] Cu is the single metal catalyst that permits C—C coupling in CO$_2$RR to form C$_{2+}$ products and nanostructuring has been shown to further enhance this
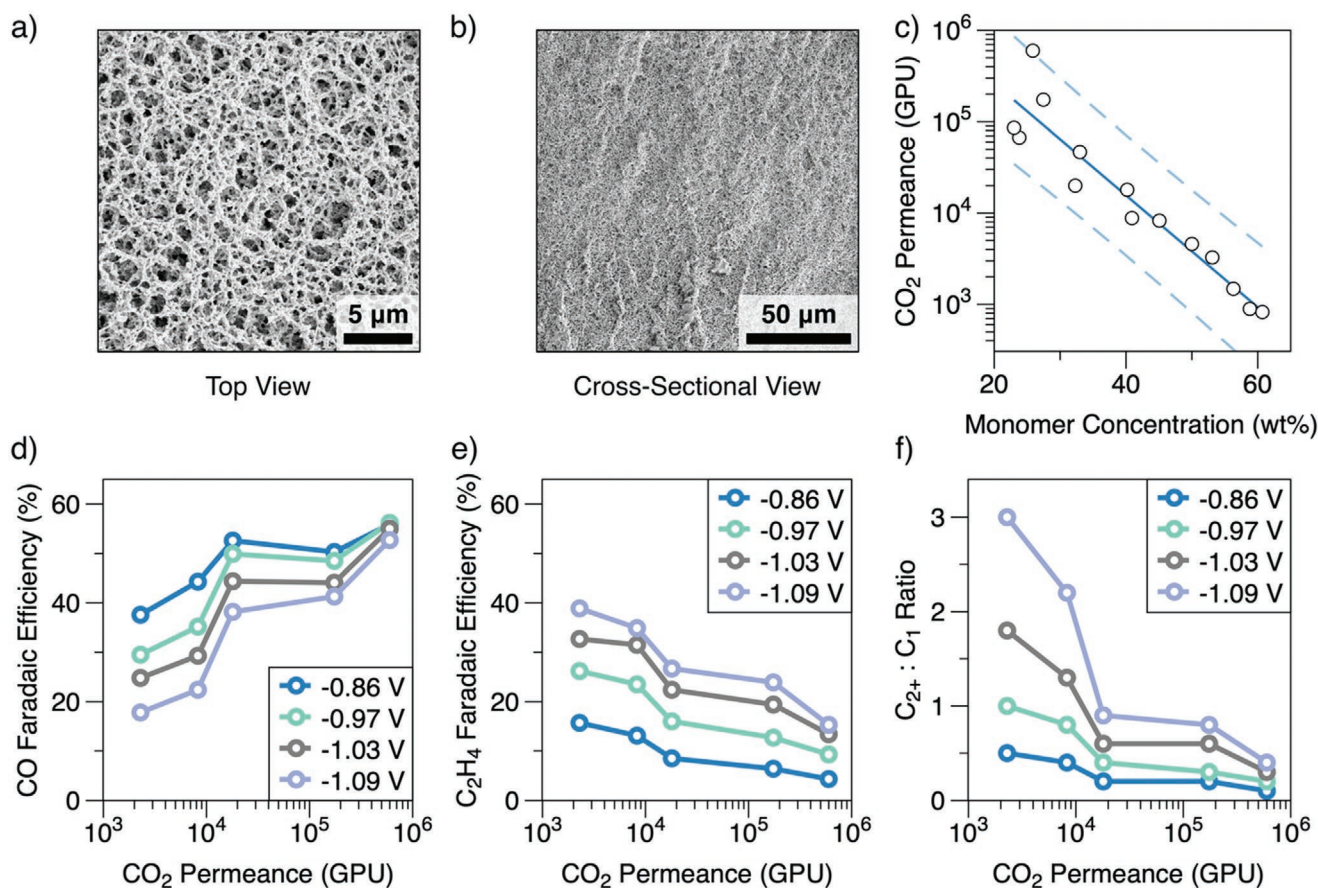
Figure 2. Permeance–performance relationship of H-PFPE. a) Top down surface and b) cross-sectional SEM images of H-PFPE. c) Hydraulic CO$_2$ permeance compared to monomer concentration of cloud point solutions used to prepare each sample. Dashed lines represent a 90% prediction interval on the exponential fit. d) CO Faradaic efficiency, e) C$_2$H$_4$ Faradaic efficiency, and f) C$_{2+}$:C$_1$ ratio of H-PFPE samples varying CO$_2$ permeance and electrochemical potential; CO$_2$RR catalyzed on a copper nanoparticle catalyst layer, 1 M KHCO$_3$ electrolyte, and a CO$_2$ inlet flow rate of 50 sccm. Data are the average of at least three independent samples where the standard deviation is less than 10% (not shown for image clarity).
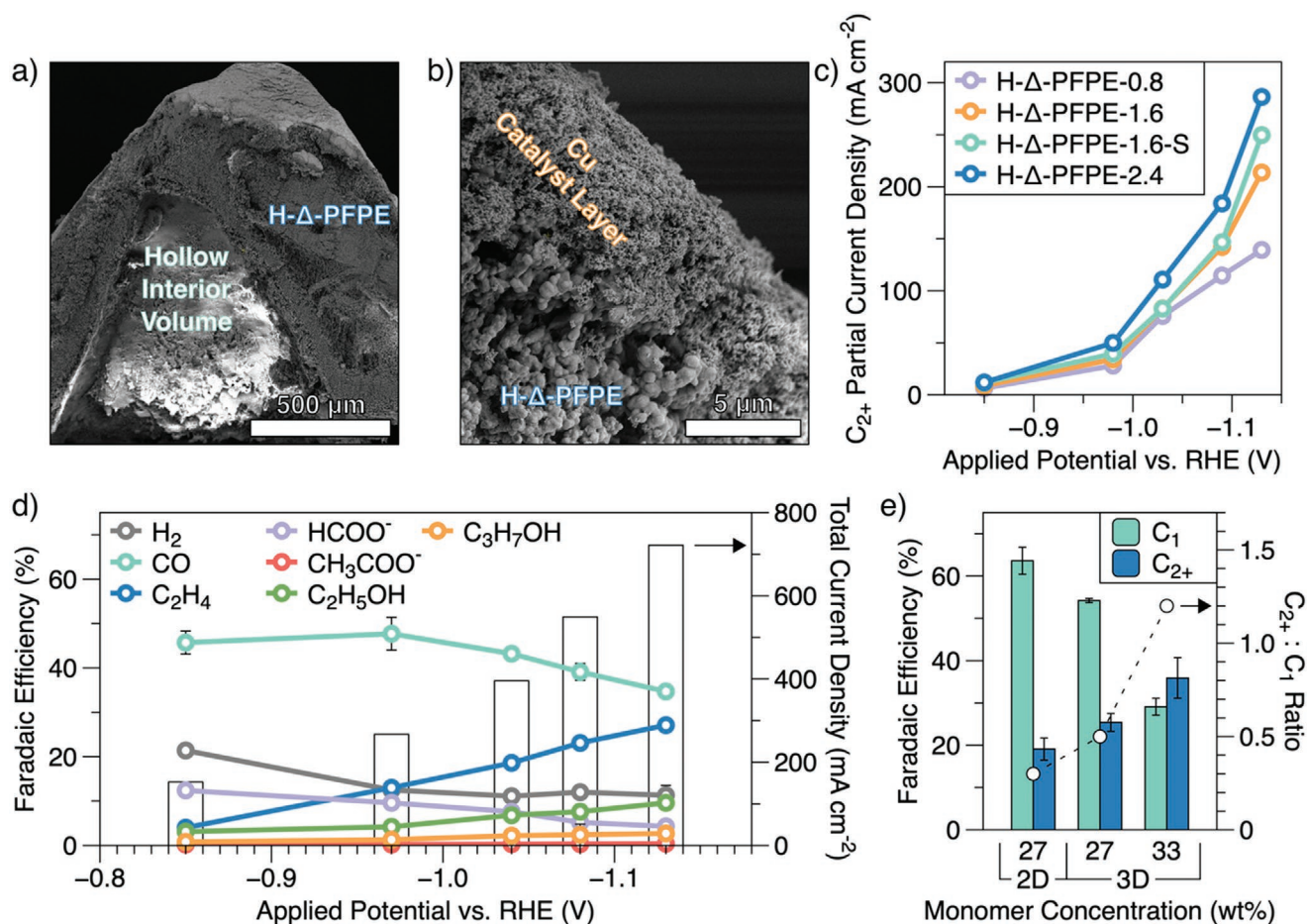
Figure 3. External Macrostructure of H-Δ-PFPE. Cross-sectional SEM images of a) a single pyramid and b) the GDL:CL interface. c) Partial current densities for C_{2+} products for the H-Δ-PFPE varying height and configuration series. d) Full product distribution of H-Δ-PFPE-2.4 and total current densities for five applied potentials. Error bars represent one standard deviation from a minimum of three independent samples. e) Comparison of 2D and 3D (H-Δ-PFPE-1.6) samples from the same monomer concentration and 3D samples (H-Δ-PFPE-1.6) made from different monomer concentrations.

capability.[27–31] A 4:3 mixture of 25 nm copper nanoparticles (mass loading of 3.3 mg cm^{-2}) and PFSA ionomer solution was spray-coated onto the PFPE GDLs, resulting in a ≈5 μm thick catalyst layer (**Figure 3**b and Figure S10, Supporting Information). By selecting a catalyst layer with a high uptake of CO_2,[26] we make the GDL the CO_2 transport limiting layer of the GDE, allowing us to study its impact on CO_2RR. This approach allows us to make the permeance to—rather than the permeance through—the catalyst layer the critical parameter. 1 M KHCO$_3$ electrolyte was used in all electrocatalytic experiments in this study to minimize the consumption of CO_2 from the reaction with hydroxide ions in the electrolyte and avoid any convoluting factors.[32] As previously shown with this catalyst layer, no statistically significant methane production was observed in any electrocatalytic experiments explored in this work.[26]

Under a range of electrochemical potentials from −0.86 to −1.09 V versus reversible hydrogen electrode (RHE), only GDLs with CO_2 permeances above approximately 2000 GPU (gas permeation units) allowed enough CO_2 to meet the catalyst layer and sustain CO_2RR at current densities up to 500 mA cm^{-2}. For H-PFPE with permeances below this experimental threshold tested in similar high current density regimes, no significant

quantities of gaseous products were measured at the outlet of the gas chamber, but rather large bubbles of H_2 were generated in the catholyte chamber. At high CO_2 permeances, CO production (Figure 2d) is invariable with increasing applied potential. At the lowest CO_2 permeance (2290 GPU), there is a 20% reduction in Faradaic efficiency (FE) to CO when comparing the −1.09 V versus RHE and −0.86 V versus RHE conditions. Interestingly, the FE for ethylene (Figure 2e) is increased to 39% only by using a less permeable GDL. Figure 2f utilizes the full product distribution to highlight the shift from C_1 to C_{2+} products by coupling more negative applied potentials with low permeance GDLs. This is in agreement with recent literature that explores the effects of mass transport on CO_2RR selectivity.[15,16] H-PFPE proved to be stable at −1.03 V versus RHE and ≈400 mA cm^{-2} with a 10% relative increase in C_2H_4 over 20 h of operation (Figure S17, Supporting Information).

Translating from planar to structured GDLs offers a number of potential advantages including the ability to vary flow and transport profiles, increased GDL:CL interfacial area, and the ability to create design-optimized structures.[33] As proof-of-concept designs, square pyramid arrays (Figure 1e and Figure S3, Supporting Information) were utilized to double the GDL:CL

**ADVANCED
SCIENCE NEWS**

www.advancedsciencenews.com

**ADVANCED
MATERIALS**

www.advmat.de

interfacial area while avoiding shadowing during spray-coating of the CL. These 3D-structured H-Δ-PFPE samples maintain the same highly porous skeletal microstructure as the planar H-PFPE and were fabricated from 27 wt% monomer solutions to achieve high permeances comparable to ePTFE. We prepared three arrays (Figure S3, Supporting Information) with different pyramid heights to study the effect of macrostructure and deviation from planar GDLs: H-Δ-PFPE-0.8 (0.8 mm tall, Figure S3e, Supporting Information), H-Δ-PFPE-1.6 (1.6 mm tall, Figure S3c, Supporting Information), and H-Δ-PFPE-2.4 (2.4 mm tall, Figure S3d, Supporting Information). Additionally, a staggered configuration with a 50% offset in the pyramid centers (H-Δ-PFPE-1.6S, 1.6 mm tall, Figure S3b, Supporting Information) was created to investigate the influence of catholyte flow over the GDL. We employed continuum simulations (detailed description in Figure S13 in the Supporting Information) to model the coupled, convective-diffusive mass transfer of a tracer diffusing into a flowing stream of fluid. This is a simplified representation of the diffusion of locally produced CO species to elucidate mass transfer at the surface, in the absence of any further reactions. The mass transfer is characterized by the Sherwood number (Sh) and is inversely related to surface concentration. A strong positional variation in Sh is predicted from the pyramids with local minima in the valleys. Taken together, the increase in interfacial area when translating from 2D to 3D GDLs and the positional variation in Sh motivate the experimental validation of structured H-Δ-PFPE performance.

The same uniformly conformal copper catalyst layer (≈5 μm) utilized in Figure 2 is depicted in Figure 3a,b on a H-Δ-PFPE GDL. Figure 3c shows the relative increase to C_{2+} production with an increase in pyramid height. This is attributed to the increase in interfacial area between the GDL and CL. In fact, comparing H-Δ-PFPE-1.6 to H-Δ-PFPE-2.4 and the corresponding nominal 1.38× increase in interfacial area, we observe a 1.36× increase in C_{2+} partial current density. By staggering the pyramid positions with H-Δ-PFPE-1.6S, we observe minimal changes to the partial current density trend, suggesting that the disruption of the catholyte flow path is less critical to the reaction than initially predicted. Figure 3d shows the full product distribution of H-Δ-PFPE-2.4 and highlights a total current density of 720 mA cm^{-2}, the highest achieved in this work. Figure 3e shows a slight improvement in the $C_{2+}:C_1$ ratio when moving from planar to 3D, when all other parameters are fixed. We observe a synergistic effect when combining a lower permeance, due to a higher monomer concentration in the PFPE synthesis, and a pyramid structure to increase the $C_{2+}:C_1$ ratio threefold over the planar equivalent under the same reaction conditions.

Porosity, macrostructure, and resulting gas transport are not the only parameters available to the PFPE material space. Serendipitously, we found, during the development of H-PFPE, that curing conditions dramatically alter the surface morphology of the material.[34] A strikingly different microstructure was created when much higher intensity UV light (200 mW cm^{-2}, 405 nm) was used to cure the ternary solutions. This large pore PFPE (LP-PFPE, **Figure 4** and Figure S6, Supporting Information) is characterized by a multiphasic and bi-continuous microstructure with a dense surface layer punctuated with pores. It is

likely that the high intensity light causes the photoinitiator to more effectively decompose, leading to faster polymerization and polymerization induced phase separation.[35,36] Surprisingly, both H-PFPE and LP-PFPE made from the same solution have almost identical CO_2 permeances (1.74×10^5 GPU vs 1.71×10^5 GPU, respectively) despite their substantial differences in surface porosity, internal microstructure, and pore volume distribution. Gas transport is hypothesized to only occur through the void space in and around the connected globules in LP-PFPE but not through the sponge-like closed-cell foam (blue arrows in Figure 4b,c) and to escape through the regions where the discretized surface pores overlap with the more open substructure underneath (Figure S7b, Supporting Information). This combination of partitioned bulk and surface morphologies results in a more uneven distribution of gaseous species to and from the catalyst layer compared to H-PFPE without starving the catalyst of CO_2. The CO_2RR product distribution in Figure 4e highlights how the microstructure and surface porosity influence the types of reactions favored. With the same catalyst layer deposited, LP-PFPE more than doubles the C_2H_4 FE and significantly minimizes that of CO for similar total current densities at −1.03 V versus RHE compared to the equivalent H-PFPE. In fact, the ratio between C_2H_4 and CO shows a 103× increase when −1.09 V versus RHE is applied.

The influence of surface morphology on transport was investigated computationally as well.[37,38] A 3D diffusion model was developed to explore gas diffusion at the GDL:CL interface for a variety of surface structures. Detailed model development is described in the Supporting Information. In this steady-state simulation, a CO tracer is generated at the triple point interface with a constant molar surface flux and then must either diffuse into the catholyte or exit the domain through the GDL as characterized by its permeance. This is an idealized situation where CO is generated at the catalyst and does not proceed through further reactions. Figure 4e,f shows the normalized tracer concentration on a model GDL surface with a discretized pore. The pore is considered a circular domain of defined permeance surrounded by a region of solid polymer with its own permeance. The ratio of mass transfer into the pore relative to the solid polymer surface is expressed as $\alpha = \frac{k_{mpore}}{k_m}$, where k_m is the mass conductance assuming a linear resistance model for diffusion within the GDL. Thus, an α of 1 corresponds to a homogeneous, uniformly conductive surface as hypothesized for H-PFPE. As the pore becomes relatively more permeable than the solid surface (α increases), a steep concentration gradient develops that produces a step change in concentration at the pore edge as highlighted in Figure 4e,f. The diffusion simulation domain is further extended away from the GDL surface as shown in Figure S14 (Supporting Information). These high α simulations are intended to reflect transport in LP-PFPE GDLs, although the exact value of α is not experimentally known. Overall, the presence of high concentration gradients and local regions of low diffusivity suggest that an increased CO residence time near the catalyst is enabled by LP-PFPE over H-PFPE materials. Increasing the residence time of locally-produced CO within the catalyst layer with LP-PFPE GDLs gives rise to the high $C_{2+}:C_1$ and $C_2H_4:CO$ ratios of 19 and 60, respectively—the highest from the PFPE
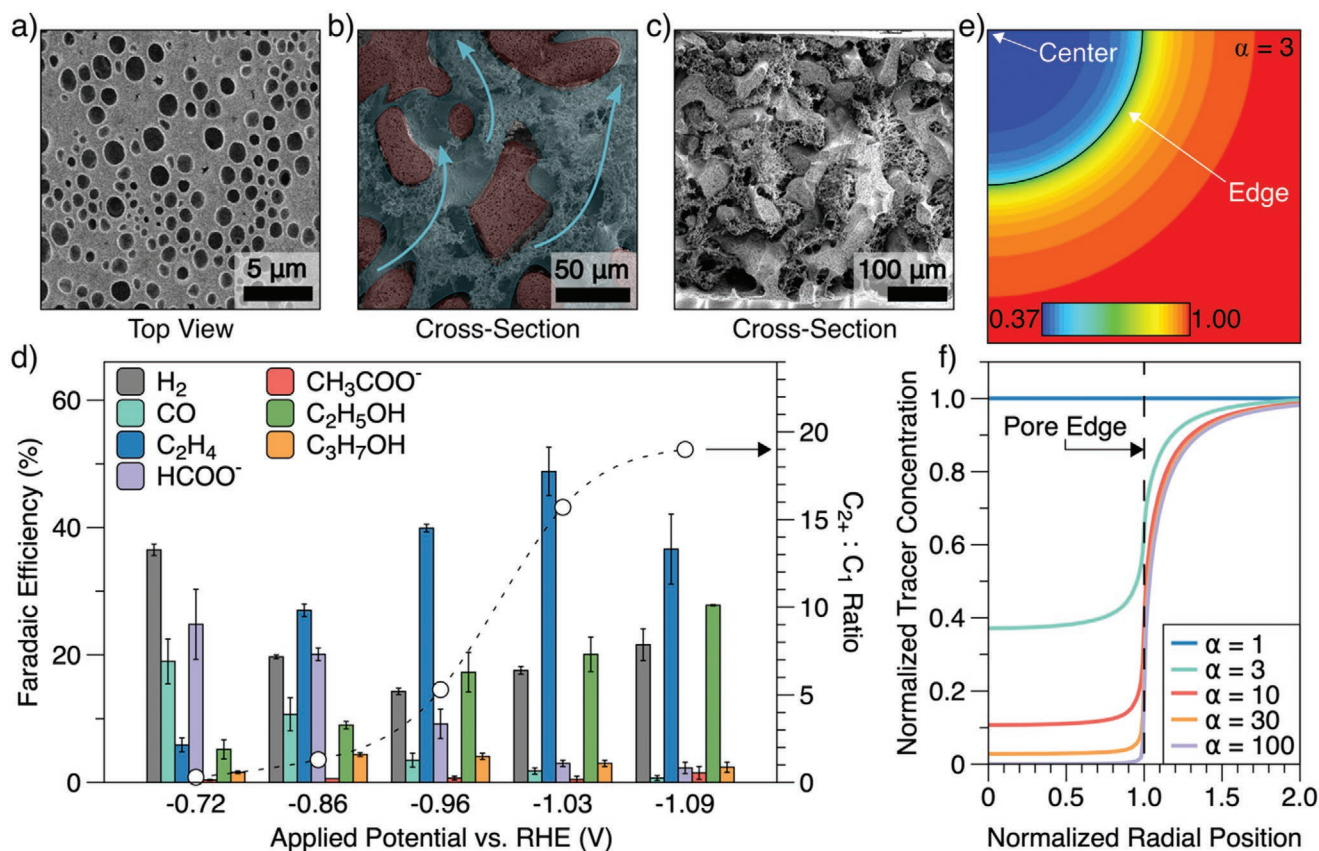
Figure 4. Surface Morphology of LP-PFPE. a) Top down surface and b,c) cross-sectional SEM images of LP-PFPE made from 33 wt% PFPE. Colored overlay in b) represents regions of high (light blue) and low (red) gas diffusion. d) Full product distribution of copper catalyst layer on LP-PFPE in 1 M KHCO$_3$ and with a 50 sccm inlet CO$_2$ flow. Error bars represent one standard deviation from a minimum of three independent samples. e) Heat map of normalized surface concentration for $\alpha = 3$, where α is the relative ratio of the mass transfer coefficient into the pore compared to the rest of the surface. f) Normalized concentration at the LP-PFPE surface consisting of a pore opening in a solid polymer.

material system—at –1.09 V versus RHE and a total current density of 420 mA cm^{-2}. Adapting this surface morphology to a 3D-structured LP-Δ-PFPE GDL proved to be an interesting counterexample (Figure S12, Supporting Information). All tested variations of the LP-Δ-PFPE GDL resulted in larger surface pores that were significantly further apart than the planar LP-PFPE. Despite the similarly high CO$_2$ permeance, the large pore spacing in the LP-Δ-PFPE did not effectively distribute the CO$_2$ to the catalyst and resulted in reactant starved operating conditions.

In summary, this work is the first account of 3D-printable porous fluoropolymers for use as next-generation GDLs. Ternary PFPE mixtures were developed and fabricated into highly gas-permeable, yet hydrophobic materials with unprecedented multiscale structural control. Variation in the surface morphology, and thus the distribution of gas, was shown to shift the product selectivity towards C$_{2+}$ products, likely by increasing the diffusive path length and residence time of locally produced CO near the catalyst. Additionally, modifying the external morphology to create 3D structures favored C$_{2+}$ products compared to their planar equivalents and enabled higher partial current densities. The results show that modulating gas transport to and from the catalyst during CO$_2$RR through gas diffusion layer design has significantly more

influence on the product distribution than previously known. Understanding how tailoring the morphology of the GDE on multiple length scales offers new insights into utilizing CO$_2$ to create value-added products.

Experimental Section

Gas Diffusion Layer Fabrication: GDLs were fabricated from ternary solutions of difunctional perfluoropolyether urethane methacrylate monomer Fluorolink MD700, *N*-methyl-2-pyrrolidone (NMP), and triethylene glycol (TEG). 2-Hydroxy-2-methylpropiophenone (Irgacure 1173) and ethyl phenyl(2,4,6-trimethylbenzoyl)phosphinate (GENOCURE* TPO-L) were used as photoinitiators. Planar GDLs were formed by placing the solution between glass plates separated by a 500 μm thick rubber gasket and held together with binder clips. The assembly was UV cured for 2 min on each side with 5 mW cm^{-2} 365 nm (H-PFPE) or 200 mW cm^{-2} 405 nm (LP-PFPE) UV light. Pyramid-structured GDLs (H-Δ-PFPE) were fabricated using either the custom-built Large Area Projection Microstereolithography (LAPμSL) printer with a 405 nm UV digital light projection source[39,40] or by curing the solution in silicone molds produced from 3D-printed casings (Formlabs Form 2). H-Δ-PFPE GDLs created by each method exhibited equivalent structure and transport properties and were used interchangeably. LP-Δ-PFPE GDLs were created in silicone molds only. Cured GDLs were placed in polypropylene tissue processing capsules before solvent exchange in acetone and supercritical drying (E3000, Polaron).

Gas Permeation Measurements: GDL permeance was measured in a custom-built isobaric gas permeation system.[41] Membrane samples were mounted onto 127 µm thick polyimide frames (Kapton HN, DuPont) with silicone glue (734 Flowable Adhesive Sealant, Dow Corning) and placed in a dead-end permeation cell. The feed consisted of room temperature (21 °C) CO_2 and the permeate flow rate was measured with mass flow meters.

Electrode Preparation: The catalyst layer was composed of a mixture of 25 nm Cu nanoparticles and Nafion ionomer (1100 EW). A nominal mass loading of 3.33 mg cm^{-2} was used in a 4:3 ratio of Cu to Nafion ionomer perfluorinated resin solution. The mixture was dispersed in methanol and sonicated for at least 1 hour before spray-coating the GDL of interest.

CO_2 Reduction Experiments: All electrochemical reduction experiments were conducted in a flow cell reactor, as depicted in Figure 1a. An Autolab PGSTAT302N Potentiostat was used to apply a constant electrical potential, which was referenced to a 3 M KCl-filled Ag/AgCl reference electrode. 1 M $KHCO_3$ electrolyte was used as the electrolyte in all electrochemical experiments. CO_2 was delivered to the reactor at a rate of 50 sccm. Outlet gas flow was measured manually using a bubble flowmeter. A Fumasep FAA-3-PK-130 anion exchange membrane (AEM) and nickel foam anode completed the electrochemical cell. Series resistance R_s was determined by electrochemical impedance spectroscopy (EIS). Gas products were quantified using gas chromatography (Perkin Elmer 600). Ethylene and methane were measured with a flame ionization detector (FID) and a thermal conductivity detector (TCD) was used for hydrogen and carbon monoxide determination. A 600 MHz Agilent DD2 1H NMR spectrometer with water suppression was used to measure the liquid products after running the reaction for at least 20 minutes.

Supporting Information

Supporting Information is available from the Wiley Online Library or from the author.

Acknowledgements

Conflict of Interest

The authors declare no conflict of interest.

Keywords

[1] M. Jouny, W. Luc, F. Jiao, *Ind. Eng. Chem. Res.* **2018**, *57*, 2165.
[2] P. De Luna, C. Hahn, D. Higgins, S. A. Jaffer, T. F. Jaramillo, E. H. Sargent, *Science* **2019**, *364*, 534.
[3] W. A. Smith, T. Burdyny, D. A. Vermaas, H. Geerlings, *Joule* **2019**, *3*, 1822.
[4] T. Burdyny, W. A. Smith, *Energy Environ. Sci.* **2019**, *12*, 1442.
[5] K. Yang, R. Kas, W. A. Smith, *J. Am. Chem. Soc.* **2019**, *141*, 15891.
[6] B. Endrődi, G. Bencsik, F. Darvas, R. Jones, K. Rajeshwar, C. Janáky, *Prog. Energy Combust. Sci.* **2017**, *62*, 133.
[7] P. Jeanty, C. Scherer, E. Magori, K. Wiesner-Fleischer, O. Hinrichsen, M. Fleischer, *J. CO2 Util.* **2018**, *24*, 454.
[8] C. M. Gabardo, C. P. O'Brien, J. P. Edwards, C. McCallum, Y. Xu, C.-T. Dinh, J. Li, E. H. Sargent, D. Sinton, *Joule* **2019**, *3*, 2777.
[9] J. Li, G. Chen, Y. Zhu, Z. Liang, A. Pei, C.-L. Wu, H. Wang, H. R. Lee, K. Liu, S. Chu, Y. Cui, *Nat. Catal.* **2018**, *1*, 592.
[10] L. Cindrella, A. M. Kannan, J. F. Lin, K. Saminathan, Y. Ho, C. W. Lin, J. Wertz, *J. Power Sources* **2009**, *194*, 146.
[11] R. Omrani, B. Shabani, *Int. J. Hydrogen Energy* **2017**, *42*, 28515.
[12] J. Lee, S. Chevalier, R. Banerjee, P. Antonacci, N. Ge, R. Yip, T. Kotaka, Y. Tabuchi, A. Bazylak, *Electrochim. Acta* **2017**, *236*, 161.
[13] S. C. Perry, S. M. Gateman, R. Malpass-Evans, N. McKeown, M. Wegener, P. Nazarovs, J. Mauzeroll, L. Wang, C. Ponce de León, *Chemosphere* **2020**, *248*, 125993.
[14] X. Wang, Z. Wang, F. P. García de Arquer, C.-T. Dinh, A. Ozden, Y. C. Li, D.-H. Nam, J. Li, Y.-S. Liu, J. Wicks, Z. Chen, M. Chi, B. Chen, Y. Wang, J. Tam, J. Y. Howe, A. Proppe, P. Todorović, F. Li, T.-T. Zhuang, C. M. Gabardo, A. R. Kirmani, C. McCallum, S.-F. Hung, Y. Lum, M. Luo, Y. Min, A. Xu, C. P. O'Brien, B. Stephen, B. Sun, A. H. Ip, L. J. Richter, S. O. Kelley, D. Sinton, E. H. Sargent, *Nat. Energy* **2020**, *5*, 478.
[15] F. L. P. Veenstra, N. Ackerl, A. J. Martín, J. Pérez-Ramírez, *Chem* **2020**, *6*, 1707.
[16] Y. C. Tan, K. B. Lee, H. Song, J. Oh, *Joule* **2020**, *4*, 1104.
[17] B. Kim, F. Hillman, M. Ariyoshi, S. Fujikawa, P. J. A. Kenis, *J. Power Sources* **2016**, *312*, 192.
[18] M. Jouny, W. Luc, F. Jiao, *Nat. Catal.* **2018**, *1*, 748.
[19] X. Wang, J. F. de Araújo, W. Ju, A. Bagger, H. Schmies, S. Kühl, J. Rossmeisl, P. Strasser, *Nat. Nanotechnol.* **2019**, *14*, 1063.
[20] D. Helmer, N. Keller, F. Kotz, F. Stolz, C. Greiner, T. M. Nargang, K. Sachsenheimer, B. E. Rapp, *Sci. Rep.* **2017**, *7*, 15078.
[21] N. Keller, J. Bruchmann, T. Sollich, C. Richter, R. Thelen, F. Kotz, T. Schwartz, D. Helmer, B. E. Rapp, *ACS Appl. Mater. Interfaces* **2019**, *11*, 4480.
[22] C. M. Friesen, B. Améduri, *Prog. Polym. Sci.* **2018**, *81*, 238.
[23] R. Bongiovanni, A. Medici, A. Zompatori, S. Garavaglia, C. Tonelli, *Polym. Int.* **2012**, *61*, 65.
[24] S. Mazinani, S. Darvishmanesh, A. Ehsanzadeh, B. Van der Bruggen, *J. Membr. Sci.* **2017**, *526*, 301.
[25] R. Kurt, L. Simon, R. Penterman, E. Peeters, H. de Koning, D. J. Broer, *J. Membr. Sci.* **2008**, *321*, 51.
[26] F. P. García de Arquer, C.-T. Dinh, A. Ozden, J. Wicks, C. McCallum, A. R. Kirmani, D.-H. Nam, C. Gabardo, A. Seifitokaldani, X. Wang, Y. C. Li, F. Li, J. Edwards, L. J. Richter, S. J. Thorpe, D. Sinton, E. H. Sargent, *Science* **2020**, *367*, 661.
[27] A. Bagger, W. Ju, A. S. Varela, P. Strasser, J. Rossmeisl, *ChemPhysChem* **2017**, *18*, 3266.
[28] A. J. Garza, A. T. Bell, M. Head-Gordon, *ACS Catal.* **2018**, *8*, 1490.
[29] J.-J. Lv, M. Jouny, W. Luc, W. Zhu, J.-J. Zhu, F. Jiao, *Adv. Mater.* **2018**, *30*, 1803111.
[30] D. Wakerley, S. Lamaison, F. Ozanam, N. Menguy, D. Mercier, P. Marcus, M. Fontecave, V. Mougel, *Nat. Mater.* **2019**, *18*, 1222.
[31] Y.-X. Duan, F.-L. Meng, K.-H. Liu, S.-S. Yi, S.-J. Li, J.-M. Yan, Q. Jiang, *Adv. Mater.* **2018**, *30*, 1706194.
[32] M. Ma, E. L. Clark, K. T. Therkildsen, S. Dalsgaard, I. Chorkendorff, B. Seger, *Energy Environ. Sci.* **2020**, *13*, 977.
[33] S. Pawlowski, J. G. Crespo, S. Velizarov, *Int. J. Mol. Sci.* **2019**, *20*, 165.
[34] Q. Tran-Cong-Miyata, H. Nakanishi, *Polym. Int.* **2017**, *66*, 213.

[35] F. Wang, L. Ratke, H. Zhang, P. Altschuh, B. Nestler, *J. Sol-Gel Sci. Technol.* **2020**, *94*, 356.

[36] N. Tsujioka, N. Ishizuka, N. Tanaka, T. Kubo, K. Hosoya, *J. Polym. Sci., Part A: Polym. Chem.* **2008**, *46*, 3272.

[37] C. Zhu, Z. Qi, V. A. Beck, M. Luneau, J. Lattimer, W. Chen, M. A. Worsley, J. Ye, E. B. Duoss, C. M. Spadaccini, C. M. Friend, J. Biener, *Sci. Adv.* **2018**, *4*, eaas9459.

[38] W. M. Deen, *Analysis of Transport Phenomena*, Oxford University Press, New York **1998**.

[39] J. A. Jackson, M. C. Messner, N. A. Dudukovic, W. L. Smith, L. Bekker, B. Moran, A. M. Golobic, A. J. Pascall, E. B. Duoss, K. J. Loh, C. M. Spadaccini, *Sci. Adv.* **2018**, *4*, eaau6419.

[40] X. Zheng, W. Smith, J. Jackson, B. Moran, H. Cui, D. Chen, J. Ye, N. Fang, N. Rodriguez, T. Weisgraber, C. M. Spadaccini, *Nat. Mater.* **2016**, *15*, 1100.

[41] N. Bui, E. R. Meshot, S. Kim, J. Peña, P. W. Gibson, K. J. Wu, F. Fornasiero, *Adv. Mater.* **2016**, *28*, 5871.